A Study of Global Aerosol Optical Climatology with Two-Channel AVHRR Remote Sensing

AKIKO HIGURASHI

National Institute for Environmental Studies, Tsukuba, Japan

TERUYUKI NAKAJIMA

Center for Climate System Research, University of Tokyo, Tokyo, Japan

BRENT N. HOLBEN AND ALEXANDER SMIRNOV

NASA Goddard Space Flight Center, Greenbelt, Maryland

ROBERT FROUIN

Scripps Institution of Oceanography, University of California, San Diego, La Jolla, California

BERNADETTE CHATENET

Laboratoire Interuniversitaire des Systemes Atmospheríques, Universités Paris 7 et Paris 12, UMR/CNRS, Paris, France

(Manuscript received 26 February 1999, in final form 25 May 1999)

ABSTRACT

Global distributions of the aerosol optical thickness and Ångström exponent are estimated from National Oceanic and Atmospheric Administration Advanced Very High Resolution Radiometer channel-1 and -2 radiances for four months in 1990. Global distributions of those Ångström parameters are consistent with present knowledge on the distributions of desert-derived, biomass-burning, and anthropogenic pollutant aerosols obtained by ground-based and aircraft measurements. Especially, it is found that thin anthropogenic aerosols can be identified with large Ångström exponent values around the east coast of North America, Europe, and eastern Asia. Satellite-retrieved values of Ångström parameters are further compared with measured spectral optical thickness obtained by the National Aeronautics and Space Administration Aerosol Robotic Network sky radiometer network.

1. Introduction

Aerosol monitoring on the global scale is essential for evaluating the aerosol radiative effects reflecting the solar radiation back to the space (Kiehl and Briegleb 1993; Taylor and Penner 1994) and its influence on the cloud albedo (Twomey et al. 1984; Kaufman and Nakajima 1993), of which climate effect is one of the greatest uncertainties in climate modeling (IPCC 1996). The total aerosol radiative forcing has been evaluated to be almost equal but with sign opposite to that of the forcing by greenhouse gases. They, however, will not offset each other and generate a complex impact on climate (Mitchell et al. 1995; Santer et al. 1996), because the aerosol distribution in concentration and composition has strong spatial and temporal variations, causing a significant difference in their radiative forcing. Early studies of such effects have focused on anthropogenic sulfate aerosols, which are believed to exert a substantial cooling effect due to their high light-scattering efficiency (Charlson et al. 1992; Kiehl and Briegleb 1993; Taylor and Penner 1994). On the other hand, recent attention has been paid to mineral dust aerosols, especially originating from a change in land use, because of its large contribution to the atmospheric aerosol loading and its large absorption of solar radiation (Tegen et al. 1996; Li et al. 1996; Sokolik and Toon 1996).

To fully understand these climate effects of aerosols, the aerosol characteristics, such as concentration, size distribution, composition, and optical properties, have to be determined on a global scale. Measurements at ground-based stations have given us an important information

Corresponding author address: Dr. Akiko Higurashi, Atmospheric Environment Division, NIES, 16-2 Onogawa, Tsukuba, Ibaraki 305-0053, Japan.
E-mail: hakiko@nies.go.jp

about aerosol physical and chemical properties in detail, though the global-scale behavior of aerosols will not be assessed from such ground-based measurement data alone, due to the strong spatial and temporal variabilities of aerosol properties. This recognition motivates us to use satellite remote sensing techniques for evaluation of the aerosol climate forcing, since satellite retrievals can generate spatially and temporally homogeneous global distributions of aerosol parameters. Present satellite retrievals are limited, however, mainly to estimation of the aerosol optical thickness, which corresponds to the column total cross section of aerosol particles, from one or two channels of polar orbiters, for example, the National Oceanic and Atmospheric Administration's (NOAA) Advanced Very High Resolution Radiometer (AVHRR), and geostationary satellites, for example, Meteosat (Stowe et al. 1991; Durkee et al. 1991; Moulin et al. 1997a). In these algorithms, an aerosol model for deriving the aerosol optical thickness has to be assumed. Extending these algorithms, a two-channel algorithm has been developed recently for retrieving the Ångström parameters, that is, the aerosol optical thickness at wavelength of 0.5 μm and Ångström exponent, simultaneously to reproduce observed radiances in two channels (Higurashi and Nakajima 1999; Higurashi et al. 1998, manuscript submitted to *Appl. Opt.*, hereafter H98). A similar algorithm has been also developed for Advanced Earth Observing Satellite (ADEOS) Polarization and Directionality of the Earth's Reflectances (POLDER) radiometer (Goloub et al. 1999).

This two-channel algorithm, applied to NOAA AVHRR and ADEOS Ocean Color and Temperature Scanner (OCTS) radiance data, has derived characteristic distributions of small and large aerosol particles of different aerosol origins (Nakajima and Higurashi 1998). As studied in Higurashi and Nakajima (1999) and H98, however, retrievals are sensitive to many assumptions made in the algorithms, such as aerosol model, calibration constants, water vapor absorption correction, and so on. It is therefore highly necessary to study the retrieval results in detail to see if the results are reasonable compared to our knowledge of spatial and temporal distributions of aerosol characteristics. For this purpose, we present in this paper four-month analyses of Ångström parameters obtained by our two-channel algorithm. The global distribution and seasonal variation of the parameters will be obtained and discussed in detail. We will further compare the results with ground-based measurement data of aerosol optical thicknesses obtained by the National Aeronautics and Space Administration's (NASA) Aerosol Robotic Network (AERONET) sky radiometer network.

2. Procedure of satellite data analysis

We have developed a two-channel algorithm in order to derive Ångström parameters (τ_a, α) defined by the following Ångström's law:

$$\tau_{a,\lambda} = \tau_a(\lambda/\lambda_0)^{-\alpha}, \tag{1}$$

where λ and $\tau_{a,\lambda}$ are wavelength in micrometer and aerosol optical thickness at λ and τ_a is the aerosol optical thickness at a reference wavelength λ_0. There have been several proposals of the reference wavelength value, that is, 1 μm (Ångström 1961), one of satellite channel wavelengths (Goloub et al. 1999) and so on. In the present study, we adopt $\lambda_0 = 0.5$ μm, because this is one of the conventional World Meteorological Organization sunphotometer wavelengths and there are long-term records of the aerosol optical thickness around this wavelength. Since the detailed description of the retrieval algorithm is found in Higurashi and Nakajima (1999) and H98, we present in this section a brief overview of the procedure used in the present data analysis.

In this study, τ_a and α are estimated from the relationship between channel-1 and -2 radiances of *NOAA-11* AVHRR, which are calculated by an accurate yet efficient lookup table method simulating the band-averaged satellite-received radiances in atmosphere–ocean systems. We assume 1.5–0.005*i* for the aerosol refractive index and the following bimodal volume size distribution:

$$\frac{dV}{d\ \ln r} = \sum_{n=1}^{2} c_n \exp\left\{-\frac{1}{2}\left[\frac{\ln(r/r_{m,n})}{\ln s}\right]^2\right\}. \tag{2}$$

We adopt $r_{m,1} = 0.17$ μm, $r_{m,2} = 3.44$ μm, $s_1 = 1.96$, and $s_2 = 2.37$ as typical climate values of mode radii and their dispersions for accumulation and coarse mode for the size distribution. We fix these values throughout the algorithm, since it is difficult to take into account the hygroscopic process to change these parameters in our algorithm. Although τ_a and the peak ratio, γ ($=c_2/c_1$), are variables in the algorithm, τ_a and α are finally retrieved because γ is uniquely transformed to α, which is a more inherent parameter for radiation transfer processes. In practice, Ångström parameters (τ_a, α) are obtained by a regression fitting of Eq. (1) to the spectral optical thicknesses $\tau_{a,\lambda}$ at regular sunphotometer wavelengths, 0.368, 0.500, 0.675, 0.862, and 1.050 μm, in order to obtain spectrally averaged values which are relevant for climate study and also suitable for validation.

The algorithm corrects satellite-received radiances for ozone absorption using daily Total Ozone Mapping Spectrometer (TOMS) retrieval data and for water vapor absorption and surface reflectance by assuming a rough ocean surface with National Centers for Environmental Prediction objective analyses data. To avoid solar specular reflection from the ocean surface, data within a 40° half-cone angle around the specular reflectance angle are excluded from the analyses. Also, we exclude data with high wind speed at 10 m above the ocean surface, that is, $u_{10} > 12$ m s^{-1}, from the analyses to avoid the effect of reflection by foam. Upwelling radiance from ocean is neglected in the algorithm, because, according to numerical simulations, its effect is not significant to

retrievals at the wavelength of AVHRR channels 1 and 2 ($\lambda = 0.64$ and 0.83 μm) in a general range of pigments and sediments (0.01–1.0 mg m^{-3}), although this approximation will cause an underestimation of Ångström exponent for very turbid oceans. The polarization effect is taken into account in the calculation of radiances, because it spoils the wavelength dependence of radiances and thus causes a serious error in the retrieved results, especially α, which is estimated with the relationship between channel-1 and -2 radiances.

3. Comparison between satellite and ground-based measurements

a. Ground-based measurements

For studying the validity of retrieved results obtained by the present retrieval algorithm, we use AERONET dataset, although the period of comparison is different, as shown later. It was difficult for us to collect other worldwide ground-based measurement data for validation in the satellite analysis year, that is, 1990. The AERONET is a ground-based aerosol monitoring network consisting of many automatic sun–sky scanning spectral radiometer stations of which data are transmitted to the data center at NASA Goddard Space Flight Center (Holben et al. 1998). From direct solar and sky radiance data, aerosol spectral optical thicknesses at $\lambda = 0.340$, 0.440, 0.670, and 1.020 μm and size distributions are derived by an inversion algorithm of Nakajima et al. (1996). Retrieved results are opened to the public through the World Wide Web (http://aeronet.gsfc.nasa.gov:8080/). In the AERONET dataset, there are two-level data, that is, levels 1 and 2, which are real time and cloud-screened data (Smirnov et al. 1998, manuscript submitted to *Remote Sens. Environ.*), respectively.

We selected stations on an island or on a coast in AERONET dataset as listed in Table 1 and shown in Fig. 1 for comparing with satellite-derived results over the ocean. From cloud-screened daily mean spectral aerosol optical thickness at 0.340, 0.440, 0.670, and 1.020 μm at the selected stations, we calculated the aerosol optical thickness at 0.5 μm and Ångström exponent with Eq. (1). The period of the AERONET data archive is after 1994 and most stations had started after 1996. Although the period of satellite retrievals in this study, 1990, does not agree with that of AERONET ground-based measurements, we compare monthly mean values of Ångström parameters, expecting monthly mean values will reflect the mean aerosol characteristics in each region without significant dependence on the year of measurements, especially for the Ångström exponent α. Table 1 lists the monthly mean aerosol optical thickness at 0.5 μm $\tau_{a,\mathrm{gr}}$ and the Ångström exponent α_{gr} calculated from daily mean values at each station.

TABLE 1. Ångström parameter values for selected AERONET data for validation. Locations and archived periods are also shown.

Station	Lat	Long	$\tau_{a,\mathrm{gr}}$ Jan	$\tau_{a,\mathrm{gr}}$ Apr	$\tau_{a,\mathrm{gr}}$ Jul	$\tau_{a,\mathrm{gr}}$ Oct	α_{gr} Jan	α_{gr} Apr	α_{gr} Jul	α_{gr} Oct	Archived period
Bermuda	32°22′N	64°41′W	—	0.156	0.182	0.101	—	1.139	0.948	1.139	Mar–Nov 1996
Cabo Verde	16°43′N	22°56′W	0.262	0.256	0.666	0.213	0.390	0.466	0.173	0.189	Oct 1994–Jun 1995; Jan 1996–Jun 1997
Dakar	14°23′N	16°57′W	0.291	0.427	0.641	—	0.846	0.240	0.117	—	Dec 1996–Aug 1997
Dry Tortugas	24°36′N	82°47′W	—	—	0.174	—	—	0.748	—	—	Jun–Sep 1996; Jun–Sep 1997
Izana	28°18′N	16°30′W	—	—	0.042	—	—	—	0.813	—	Jun–Jul 1996
Lanai	20°49′N	156°59′W	0.052	0.079	0.063	0.087	0.280	0.381	0.697	0.520	Nov 1995–Jun 1996; Aug–Dec 1996; Jul–Sep 1997
Sandy Hook	40°26′N	73°59′W	—	—	0.317	—	—	—	1.523	—	May–Aug 1996
St. Nicolas	33°15′N	119°30′W	—	0.319	—	—	—	0.489	—	—	Apr–May 1998
Tenerife	28°01′N	16°37′W	—	—	0.193	—	—	—	0.489	—	Jun–Jul 1997
Wallops	37°56′N	75°28′W	—	—	0.300	0.109	—	—	1.475	1.014	Jul, Sep–Oct 1993; Aug–Sep 1995; Jun 1996–Aug 1997

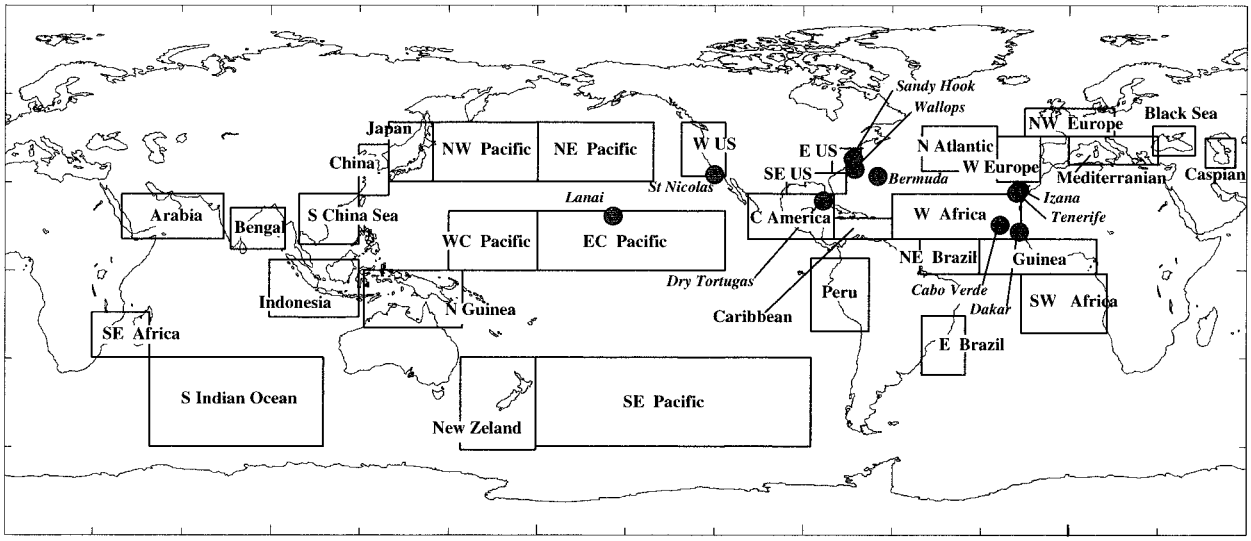

FIG. 1. Locations and names of selected AERONET stations for validation of the present satellite retrievals shown by closed circles and italic characters. Rectangles show regions for which monthly regional averages of $\tau_{a,\mathrm{sat}}$ and α_{sat} are calculated.

b. Parameter tuning

We apply the retrieval algorithm to *NOAA-11* AVHRR Global Area Coverage (GAC) data in January, April, July, and October 1990. For efficient analysis of global data, we segment the region from 60°S to 60°N into 0.5° × 0.5° lat–long boxes and bin 10 × 10 pixels into each box. A clear pixel for the analysis is selected out of the 100 pixels with the cloud-screening process of Higurashi and Nakajima (1999).

Figure 2 compares ground-based measurement values of Ångström parameters ($\tau_{a,\mathrm{gr}}$, α_{gr}) with coincident AVHRR-derived values ($\tau_{a,\mathrm{sat}}$, α_{sat}), which are averages of 5 × 5 monthly mean segment values in the region of 2.5° × 2.5° centered at the location of each station. The dispersion of the correlation is large due to disagreement of the analyzed period, especially for the retrieved results for $\alpha_{\mathrm{gr}} < 0.45$, as shown in Fig. 2. From Table 1, it is found that those small Ångström exponent values are mostly from stations influenced by Saharan dust, such as Cabo Verde and Dakar. As discussed below, there are several possible causes for the overestimation of small α (<0.45) by satellite remote sensing, such as errors involved in the calibration constants of the radiometer, the assumed aerosol model (size distribution and complex refractive index) and so on.

1) AEROSOL SIZE DISTRIBUTION

In the present algorithm, the peak volume ratio of the size distribution γ is the only adjustable parameter to describe the difference in the aerosol size distribution with fixed r_m and s for accumulation and coarse modes of the bimodal size distribution. To investigate the influence of the size distribution parameters, r_m and s, we perform sensitivity tests of channel-1 and -2 radiances of AVHRR for a change in the parameters $r_{m,1}$, $r_{m,2}$, s_1,

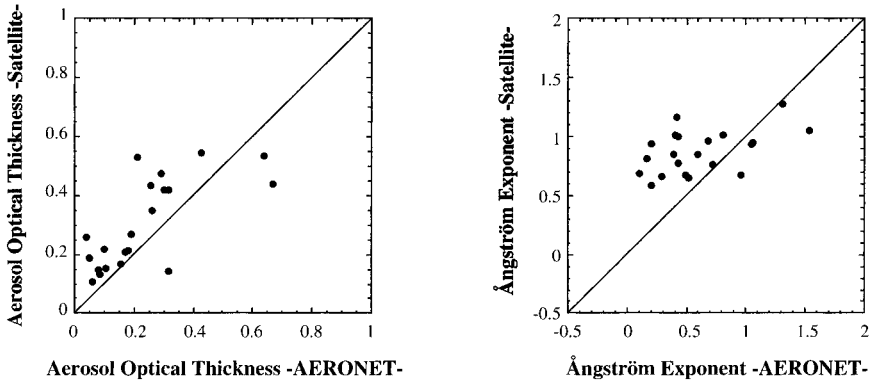

FIG. 2. The correlation between ground-based and satellite-derived τ_a and α with calibration constants case 1 and $r_{m,1} = 0.17$ μm, $r_{m,2} = 3.44$ μm, $s_1 = 1.96$, and $s_2 = 2.37$ for the assumed bimodal size distribution.

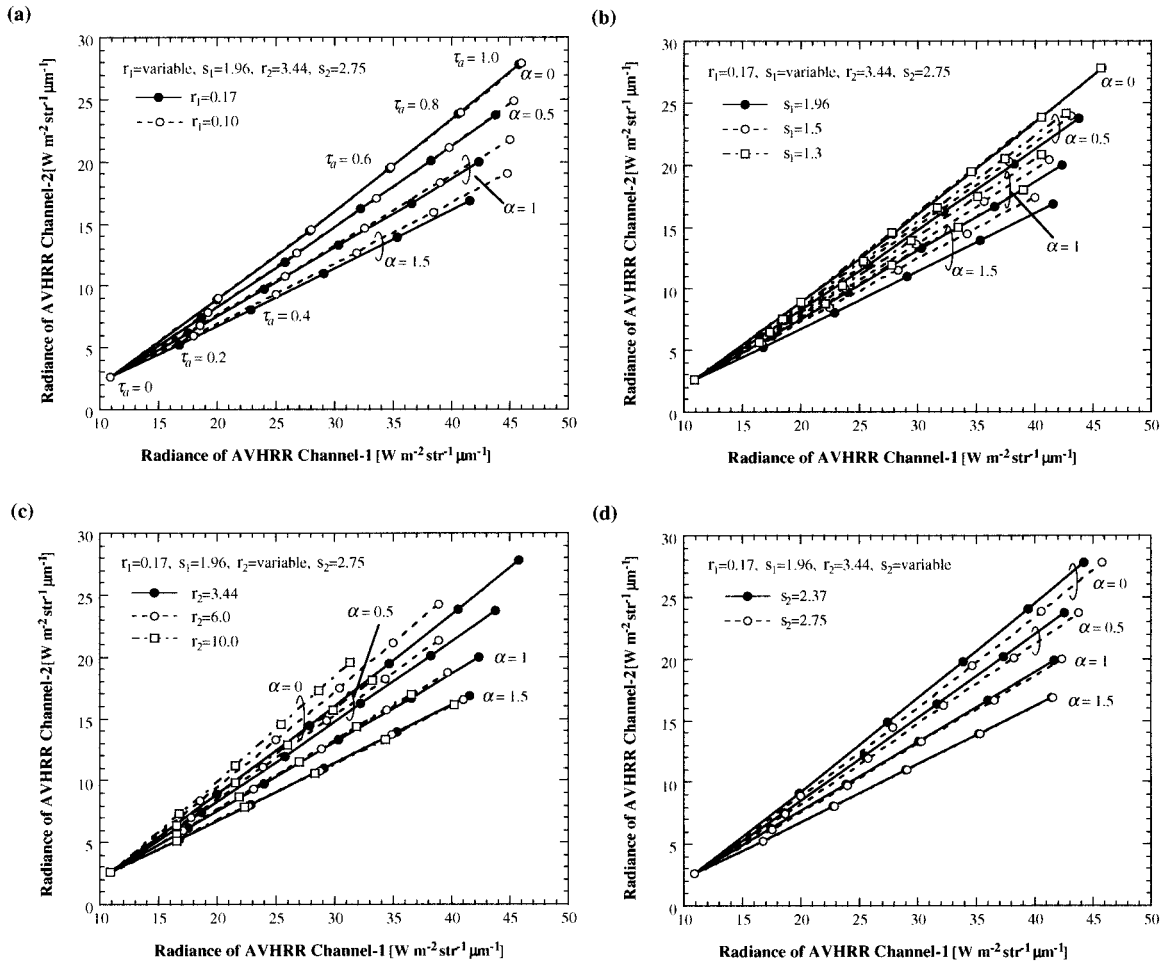

FIG. 3. Sensitivity tests with size distribution parameter changes: (a) $r_{m,1}$ = 0.10 and 0.17 μm; (b) s_1 = 1.30, 1.50 and 1.96; (c) $r_{m,2}$ = 3.44, 6.0, and 10.0 μm; (d) s_2 = 2.37 and 2.75. Other parameters are fixed at reference values as $r_{m,1}$ = 0.17 μm, s_1 = 1.96, $r_{m,2}$ = 3.44 μm, s_2 = 2.75, respectively. θ_0 = 40°, θ = 30°, ϕ = 150°; u_{10} = 7 m s^{-1}; τ_a = 0 (0.2) 1.0, α = 0 (0.5) 1.5.

and s_2. Figure 3 shows the results of four sensitivity tests for channel-1 and -2 radiances with parameter changes: $r_{m,1}$ = 0.10 and 0.17 μm; s_1 = 1.30, 1.50, and 1.96; $r_{m,2}$ = 3.44, 6.0, and 10.0 μm; and s_2 = 2.37 and 2.75. Other parameters are fixed at reference values as $r_{m,1}$ = 0.17 μm, s_1 = 1.96, $r_{m,2}$ = 3.44 μm, and s_2 = 2.75, respectively. In these calculations, we set solar zenith angle θ_0 = 40°, satellite zenith angle θ = 30°, azimuth angle ϕ = 150°, u_{10} = 7 m s^{-1}, τ_a = 0 (0.2) 1.0, and α = 0 (0.5) 1.5.

Shifting the mode radii of accumulation and coarse modes toward smaller values, radiances in both channels for the same τ_a and α increase in both cases. On the other hand, the wavelength dependence of the two-channel radiances, that is, the slope of the two-channel plot, is rather insensitive to the changes in mode radii. In order to understand this behavior, we introduce the linearized single-scattering approximation of radiances in each channel as

$$L = \frac{\omega \tau P}{\mu}, \tag{3}$$

where μ, ω, and P show the cosine of satellite zenith angle, the single scattering albedo, and scattering phase function of the atmospheric layer, respectively. Values of P in the range of scattering angles (Θ = 75°–150°) used in most of the *NOAA-11* satellite measurements increase with increasing contribution of small particles, which will be the reason for the increase in radiances with a decrease in mode radii. The wavelength dependence of radiances is mainly caused by the wavelength dependence of τ_a, which increases with increasing contribution of small particles in the test range of the radius change in Fig. 3. In case of fixed γ, a decrease in the mode radius is equivalent to an increase in the contribution of small particles, but it is not the case if α is fixed because γ has to be increased so as to keep α constant. Therefore, the expected change in the wavelength dependence in radiances is smaller in fixed-α

TABLE 2. Calibration coefficients and deep space counts for *NOAA-11* AVHRR channel 1 and 2 in 1990.

Source	S_1	$C_{0,1}$	S_2	$C_{0,2}$
Preflight	0.492	40.000	0.356	33.930
Rao and Chen (1995)	0.56 ± 0.01	40.000	0.38 ± 0.01	40.000
Kaufman and Holben (1993)	0.59 ± 0.02	40.000	0.41 ± 0.02	40.000
Che and Price (1992)	0.580	—	0.394	—
This study, case 1	0.578	38.750	0.425	39.750
This study, case 2	0.570	38.388	0.450	39.625

cases than that in fixed-γ cases. This is another reason why we selected α for a size index rather than γ, which is more directly related with the shape of the size distribution. Even though there is such an invariability, Fig. 3 indicates that the wavelength dependence of radiances for small α is sensitive to a change in the mode radius of the coarse mode.

On the other hand, the influence of increasing the dispersion of each mode is more complicated. The dispersion of the coarse mode does not noticeably affect the radiances in the large particle limit, as well known in cloud remote sensing (e.g., Nakajima and King 1990). It is interesting to see that the dispersion of the accumulation mode strongly affects the wavelength dependence of two-channel radiances for all the α values. To understand this phenomenon, we have to note typical values for the size parameter of the accumulation mode particles are 1.7 and 1.1 in the two channels, respectively, whereas the first maximum peak of the scattering efficiency factor as a function of size parameter is located around a size parameter of 4 for the refractive index assumed in this study (van de Hulst 1957). This means the scattering efficiency decreases rapidly with decreasing size parameter. Even when we fix α, that is, the wavelength dependence of τ_a, the wavelength dependence of the phase function will be affected in this process. Therefore, a difference in the dispersion of the accumulation mode size distribution makes a large change in the wavelength dependence of two-channel radiances, because the size parameter range for integration of scattering cross section changes significantly with a wavelength change.

Preceding numerical experiments show that a tuning of size distribution parameters can change retrieved values of the Ångström exponent in a complicated manner, especially with changes in the mode radius of the coarse particle mode and the dispersion of the accumulation mode. Note that the α value can decrease from 0.8 to 0.4 for a given set of two-channel radiances, for example, when we increase the mode radius of the coarse mode and decrease the dispersion of the accumulation mode.

2) CALIBRATION COEFFICIENTS OF THE AVHRR SENSOR

We begin with notations used in the calibration procedure. The spectral radiance L_i detected in channel i is related with digital count C_i as follows:

$$L_i = S_i(C_i - C_{0,i}), \tag{4}$$

where $C_{0,i}$ is the deep space count and S_i is the calibration coefficient for channel *i.* The sensor calibration is a serious problem in using satellite data, especially those that are not calibrated on board, such as data in AVHRR channels 1 and 2. Some calibration coefficients for *NOAA-11* AVHRR channels 1 and 2 have been proposed by several researchers (Che and Price 1992; Kaufman and Holben 1993; Rao and Chen 1995) as shown in Table 2. It is important to note a large variation in the reported values. In order to obtain an independent evaluation of the calibration coefficients, we plot in this study the minimum counts in each segment (a latitude–longitude box of 0.5° × 0.5°) versus theoretical values of the molecular atmosphere as shown in Fig. 4. It is found that the calibration coefficient and deep space counts may be determined by a linear regression of the minimum envelope of the plot, although the variation in the observed minimum digital counts is significantly large for such a linear regression, due to a small aerosol loading even with the minimum radiance pixels. The calibration coefficients and deep space counts labelled ''case 1'' in Table 2, which are used in the previous analysis in Fig. 2, are determined as $S_1 = 0.578$, $C_{0,1} = 38.75$, $S_2 = 0.4225$, and $C_{0,2} = 39.75$, considering Fig. 4 and past investigations. Note that the calibration coefficients are similar to values by Kaufman and Holben (1993), but deep space counts are different, especially for channel 1. Although deep space counts are thought to be stable at 40, our retrieved results have a dependence on the solar zenith angle in case of fixed deep space counts at 40. Therefore, we have determined the deep space counts by a linear regression labelled case 1 in Fig. 4 keeping the slope unchanged. On the other hand, the calibration coefficients and deep space counts labelled ''case 2'' have been simultaneously determined by the linear regression as in Fig. 4. The results with this calibration constants are shown in Fig. 5 as in Fig. 2. With increasing calibration coefficient for channel 2, radiances in channel 2 increase and, as a result, retrieved Ångström exponent values decrease regardless of the values.

The above discussion may suggest that a simultaneous tuning of the size distribution parameters and calibration constants may bring the retrieved Ångström exponent values close to the ground-based measurement values. If we adopt the calibration constants case 2, parameters of the size distribution should be modified

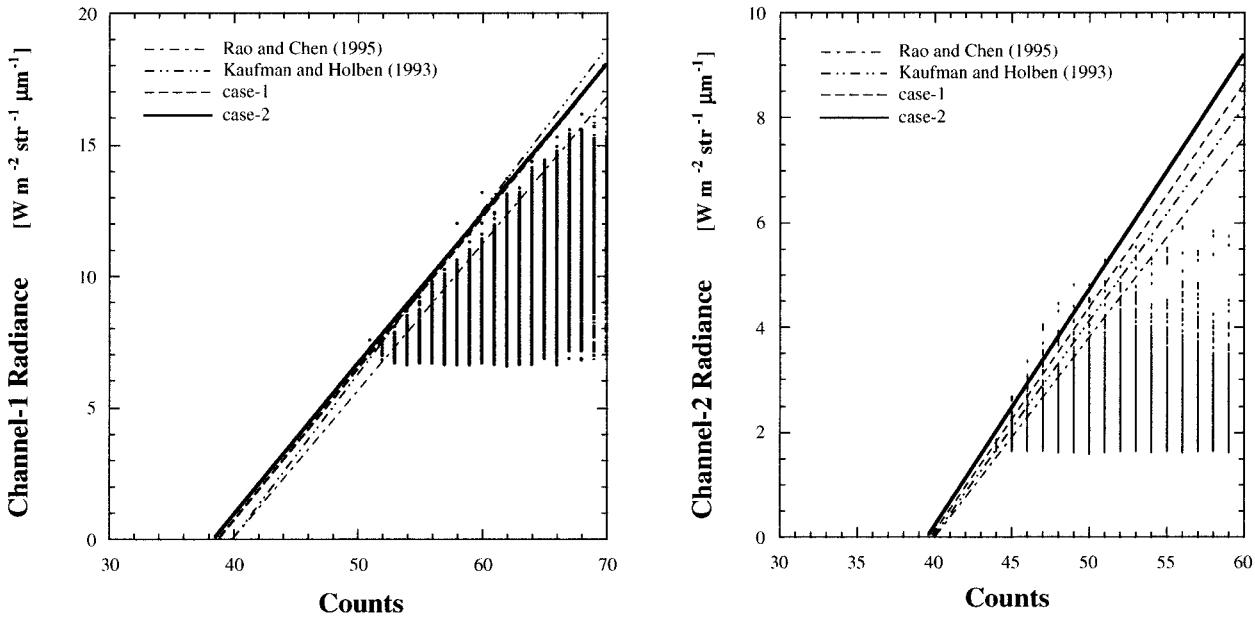

FIG. 4. The relationship between minimum digital counts in *NOAA-11* AVHRR channels 1 and 2 in each segment data and corresponding theoretical values for the molecular atmosphere.

so as to decrease α_{sat} corresponding to large α_{gr} and to increase α_{sat} for small α_{gr}. Figure 3 suggests that such a tuning can be realized by decreasing $r_{m,1}$ or s_1 and increasing s_2. Figure 6 shows the results with calibration constants case 2 and tuned size distribution parameters, $r_{m,1} = 0.17$ μm, $r_{m,2} = 3.44$ μm, $s_1 = 1.3$, and $s_2 = 2.75$, thus determined. Although α_{sat} for $\alpha_{gr} < 0.45$ are still overestimated by the present method, the agreement between them is improved compared to Fig. 2. We should attribute the remained disagreement between satellite and ground-based values to the difference in observing periods between them.

3) COMPLEX REFRACTIVE INDEX

Another issue for improving the retrieval results is the assumption of complex refractive index, especially for mineral dust aerosol cases in which we had a large disagreement between satellite and ground-based observation as shown in Figs. 2, 5, and 6. We assumed 1.5–0.005*i* for the aerosol complex refractive index, supposing the mean refractive index of absorbing and nonabsorbing aerosols. In the NOAA phase-1 operational algorithm, the aerosol complex refractive index is assumed at 1.5–0.0*i*, whereas Ignatov et al. (1995) have pointed out that this value is not suitable and proposed 1.5–0.01*i* for channel 1 from a validation using sunphotometer measurements off the west coast of North Africa and in the Mediterranean Sea. Moulin et al. (1997a) also proposed 1.5–0.01*i* for a desert aerosol model from a comparison between Meteosat-derived ($\lambda = 0.7$ μm) and sunphotometer-derived aerosol optical thicknesses. On the other hand, the imaginary part of

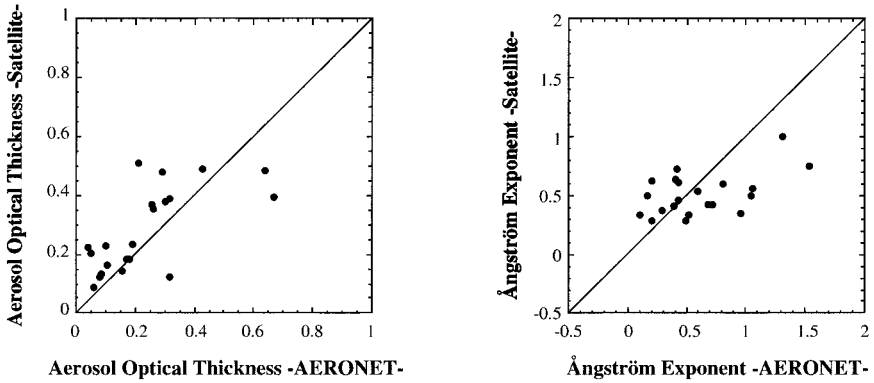

FIG. 5. Same as in Fig. 2, but with calibration constants case 2, $r_{m,1} = 0.17$ μm, $r_{m,2} = 3.44$ μm, $s_1 = 1.96$, and $s_2 = 2.37$ for bimodal size distribution, and complex refractive index of 1.5–0.005*i*.

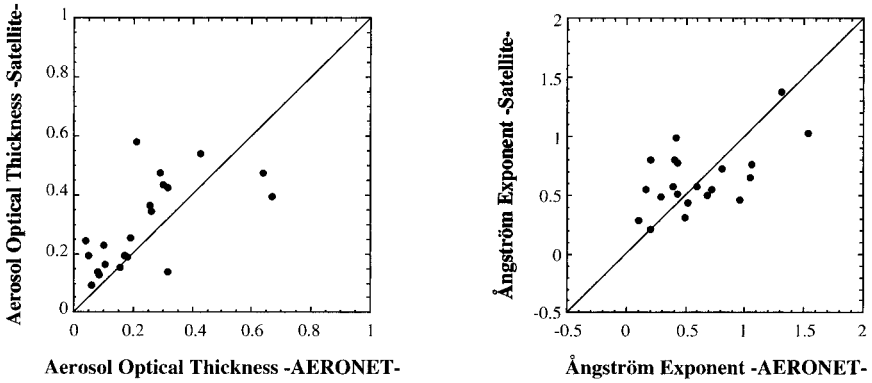

FIG. 6. Same as in Fig. 2, but with calibration constants case 2, $r_{m,1} = 0.17$ μm, $r_{m,2} = 3.44$ μm, $s_1 = 1.3$, and $s_2 = 2.75$ for bimodal size distribution, and complex refractive index of 1.5–0.005*i*.

the complex refractive index for desert dust obtained by ground-based measurements is 0.005 $\pm$ 0.002 in the spectral range from 0.5 to 1.0 μm with some wavelength dependence (Sokolik et al. 1993; Patterson et al. 1977; Carlson and Caverly 1977; Tomasi et al. 1983). These studies suggest that our assumption of 1.5–0.005*i* is suitable for remote sensing of dust aerosols as a first approximation. More detailed study of the ground-based measurement values shows, however, that the imaginary part of refractive index of Saharan dust has a sharp decrease and takes the minimum value around 0.6–0.7 μm and then slowly increases for longer wavelengths. According to this fact, it may be better to assume an imaginary index for channel 2 larger than that for channel 1. Figure 7 shows the results with the same parameters as in Fig. 6 but with an imaginary index for channel 2 as 0.006 for the cases of $\alpha_{gr} < 0.45$ in Fig. 6. The increase of the imaginary index for channel 2 improves the agreement of α_{sat} with $\alpha_{gr} < 0.45$.

This experiment suggests that the retrievals are improved if the imaginary index in channel 2 is increased selectively for mineral dust aerosols. Neglecting the spectral dependence of the complex refractive index may be one of reasons of disagreement between satellite-derived and ground-based Ångström exponents for mineral dust practices.

4) CLOUD SCREENING

Cloud screening is one of the important issues in improving the accuracy of retrieved aerosol optical properties; it has to be done carefully because it may cause underestimation of aerosol effects due to removing thick aerosol layers in mistake for cloud one.

We select clear pixels from segment data, which are made from AVHRR GAC data and have 10 $\times$ 10 pixels in each 0.5° $\times$ 0.5° lat–long box, as follows: 1) exclude the segment if it does not have more than 40 pixels with channel-1 reflectance less than 0.45 and channel-4 brightness temperature larger than 270 K; 2) exclude the segment if the 30th lowest reflectance in channel 1 exceeds 0.2; 3) exclude the segment if the root-mean-square deviation of third through 15th lowest reflectances in channel 1 exceeds 0.02; and 4) select the pixel with the third lowest reflectance in channel 1.

Figure 8 shows the correlation between AVHRR-derived Ångström parameters and ground-based values of real-time data without cloud screening. It is interesting

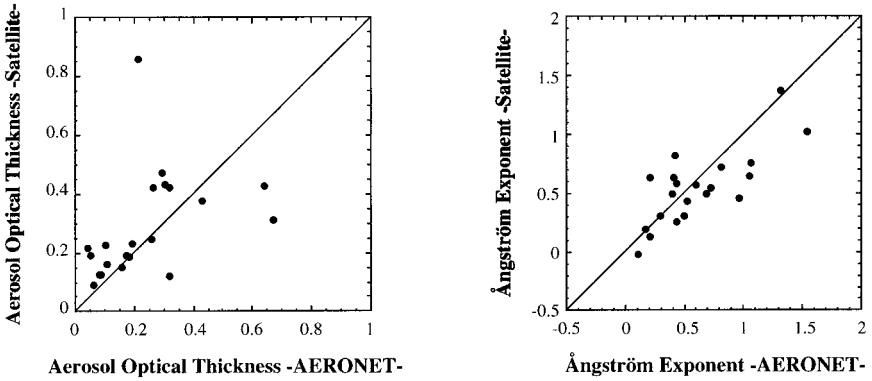

FIG. 7. Same as in Fig. 6 but with a complex refractive index for channel 2 as 1.5–0.006*i* for the cases of $\alpha_{gr} < 0.45$ in Fig. 6.

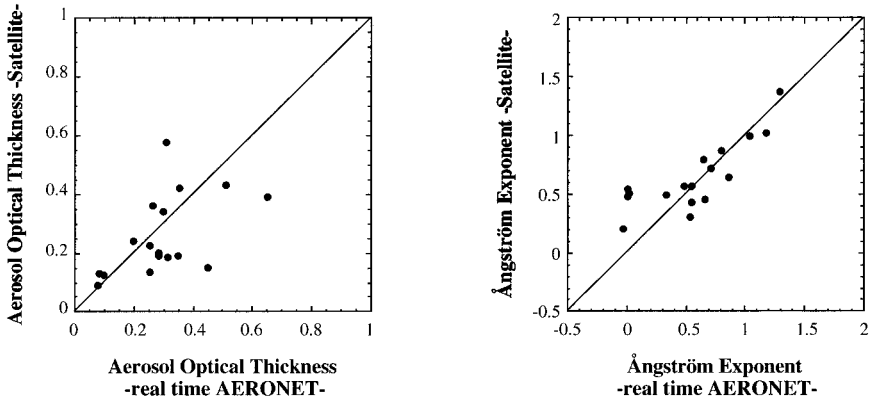

FIG. 8. Same as in Fig. 6 but with real-time ground-based τ_a and α.

to see a better correlation compared to Fig. 6 for both Ångström coefficient and exponent. In particular, the dispersion of the Ångström exponent is significantly reduced except for very small ground-based values. Figure 9 shows the correlation between monthly mean Ångström parameters with and without cloud screening for AERONET aerosol optical thicknesses at the stations and the period listed in Table 1. Cloud-screened AERONET aerosol optical thicknesses are significantly smaller than or almost equal to no cloud-screened ones, resulting in a monthly mean difference of about 0.1. As for the Ångström exponent, on the other hand, most cloud-screened ones are greater than no cloud-screened values with a difference of about 0.3. Such tendencies are understandable as an effect of cloud contamination, because clouds have a large optical thickness and neutral Ångström exponent. It should be noted in this respect that Ångström parameters of mineral dust aerosol layers are also similar to those of clouds. These observations give rise to two possibilities for causing the better correlation in Fig. 8 between satellite and ground-based retrievals compared to Fig. 6: 1) An over-cloud screening in the AERONET algorithm, removing some of mineral dust aerosol data as mistakenly classified clouds, and 2) an insufficient cloud screening in the present AVHRR algorithm producing a similar cloud contamination to the satellite-derived values. More detailed investigations will be necessary to draw a clear-cut conclusion for those speculations.

c. A modified aerosol model

As a conclusion of the discussion in the preceding sections, we adopt size distribution parameters as $r_{m,1} = 0.17$ μm, $r_{m,2} = 3.44$ μm, $s_1 = 1.3$, and $s_2 = 2.75$ and calibration constants case 2, which lead to the results as shown in Fig. 6. In the present study we do not assume a wavelength dependence in the imaginary index of refraction [which is suggested in the discussion in section 3b(3)], since it is difficult for us to introduce an automatic classification of mineral dust aerosols in the process of data analyses with only two channel radiances. It will be necessary to use more spectral channels to distinguish the aerosol type automatically. Recent and future sensors, such as ADEOS OCTS, Sea-viewing Wide Field-of-view Sensor (SeaWiFS), Earth Observing System (EOS), Moderate Resolution Imaging Spectroradiometer (MODIS), and *ADEOS-2* Global Imager (GLI), which have many spectral channels in visible and near-infrared spectral regions, will make such a treatment possible.

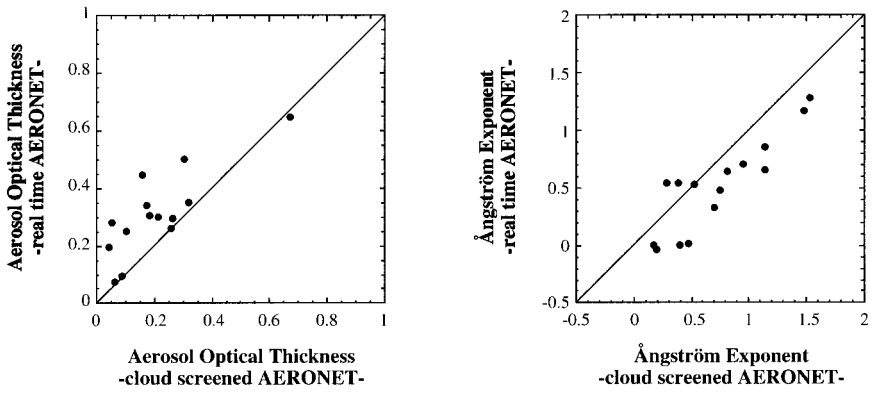

FIG. 9. The correlation of τ_a and α with and without cloud screening.

As we mentioned before, the differences still remain between satellite-derived and ground-based Ångström exponents after the modification of the aerosol model. One of the causes will be an increase of stratospheric aerosol affected by the Mt. Pinatubo eruption. We feel, however, this effect is small in the present analysis, because it has been reported that the effect of Pinatubo aerosols almost disappeared 1.5–2 yr after the eruption (Stowe et al. 1992; Yamauchi 1995). On the other hand, differences in the global circulation and the local emission strength of aerosols may cause a significant year to year variation of the Ångström parameters. In Saharan dust loading, for example, the aerosol optical thickness is strongly related to the North Atlantic Oscillation (NAO) index as suggested by Moulin et al. (1997b). It is expected, therefore, that the comparison in Fig. 6 is affected by this effect. Actually, dots with worse agreement in the aerosol optical thickness in Fig. 6 are almost from stations off the west coast of North Africa, and those in the Ångström exponent are from stations at the edge of the Saharan dust plume (e.g., Bermuda, Izana, and Tenerife) and off the large cities (Sandy Hook, Wallops, and St. Nicolas). The general overestimation of the satellite-derived aerosol optical thickness found in Fig. 6 is consistent with that the NAO index change. The NAO index value was 0.47 in 1990 and −0.01 in 1993–98, so that this difference may cause about 30% overestimation in satellite-retrieved optical thickness, which corresponds to the general trend in the comparison of Fig. 6. By this discussion it is guessed that a considerable part of the differences in Ångström parameters can be caused by differences in the sampling year.

4. Global distributions of Ångström parameters

a. Overview

Figure 10 presents the global distributions of $\tau_{a,\mathrm{sat}}$ and α_{sat} obtained from *NOAA-11* AVHRR with the present two-channel retrieval algorithm in January, April, July, and October 1990. Note that compared to the results of Higurashi and Nakajima (1999) the results show more detailed features of aerosol characteristics with longer averaging time and finer spatial binning resolution.

Distributions of $\tau_{a,\mathrm{sat}}$ in Fig. 10 show the most noticeable contribution to the aerosol loading is caused by mineral dust aerosols. We find a large quantity of mineral dust aerosols off the west coast of North Africa through the year and over the Arabian Sea in July. Saharan dust is transported over the North Atlantic Ocean by the trade winds and reaches the Caribbean Sea in July. Small α values in these regions consist with this fact, because a small α indicates a large contribution of coarse particles. Large $\tau_{a,\mathrm{sat}}$ are also found off the west coast of South Africa in July and October, which are caused by an influence of biomass burning as Herman et al. (1997) pointed out from analyses of *Nimbus-7* TOMS data. A remarkable feature seen in the distributions of α_{sat} is that large α_{sat} appear in the northern midlatitudes, in which most anthropogenic aerosol emissions are concentrated, especially off the coast of eastern North America, Europe, and eastern Asia, in April and July. This seasonal dependence is reasonable since submicron accumulation mode particles are actively generated by gas-to-particle conversion processes in summer season in these regions. We also find large α_{sat} in Central America in April. This phenomenon agrees with the fact that the biomass burning occurs in Central America in spring as reported by NASA space shuttle observation (Andreae 1993).

b. Regional features of aerosol optical properties

To understand the aerosol optical properties further, we discuss seasonal variabilities of τ_a and α, and their correlation in each region illustrated in Fig. 1. Note these regions are same as in Husar et al. (1997). The regional monthly means of $\tau_{a,\mathrm{sat}}$ and α_{sat}, in January, April, July, and October, and the four-month averages are shown in Table 3.

1) The open seas

In this study, we regard the regions as open seas labelled as NE Pacific, NW Pacific, EC Pacific, WC Pacific, SE Pacific, N Atlantic, S Indian Ocean, and New Zealand in Fig. 1.

The variability of $\tau_{a,\mathrm{sat}}$ is small over the open seas, especially in the Southern Hemisphere, compared to in other regions, while α_{sat} increases in spring and summer seasons. Correlations between $\tau_{a,\mathrm{sat}}$ and α_{sat} in the regions SE Pacific, NW Pacific, and N Atlantic are shown in Fig. 11. Figure 11a shows α_{sat} initially increases with increasing $\tau_{a,\mathrm{sat}}$ and then decreases with further increases of $\tau_{a,\mathrm{sat}}$ exceeding 0.2–0.4 in spring and summer. The peak reaches a value close to 1. Since the atmosphere over the open sea is usually expected to be affected mostly by oceanic aerosols, the correlation patterns mentioned above may be caused by accumulation and growth processes of sulfate particles generated by ocean biological activities. Actually, gas-to-particle conversion and accumulation process of aerosols cause an increase in both τ_a and α, that is, a positive correlation, whereas a growth process of aerosols absorbing water vapor causes an increase in τ_a and a decrease in α, that is, a negative correlation (Nakajima et al. 1989; Kaufman and Holben 1996). A typical α value associated with those processes is around 1. On the other hand, the broad negative correlation with small α_{sat} values in Fig. 11 may be attributed to the growth process of sea salt particles. Typical sea salt particles are much larger than gas-to-particle conversion aerosols and are associated with a values close to 0 (Gordon and Wang 1994).

An influence of anthropogenic aerosol emissions also may not be ignored even over the open sea in the Northern Hemisphere, especially in the North Atlantic Ocean,

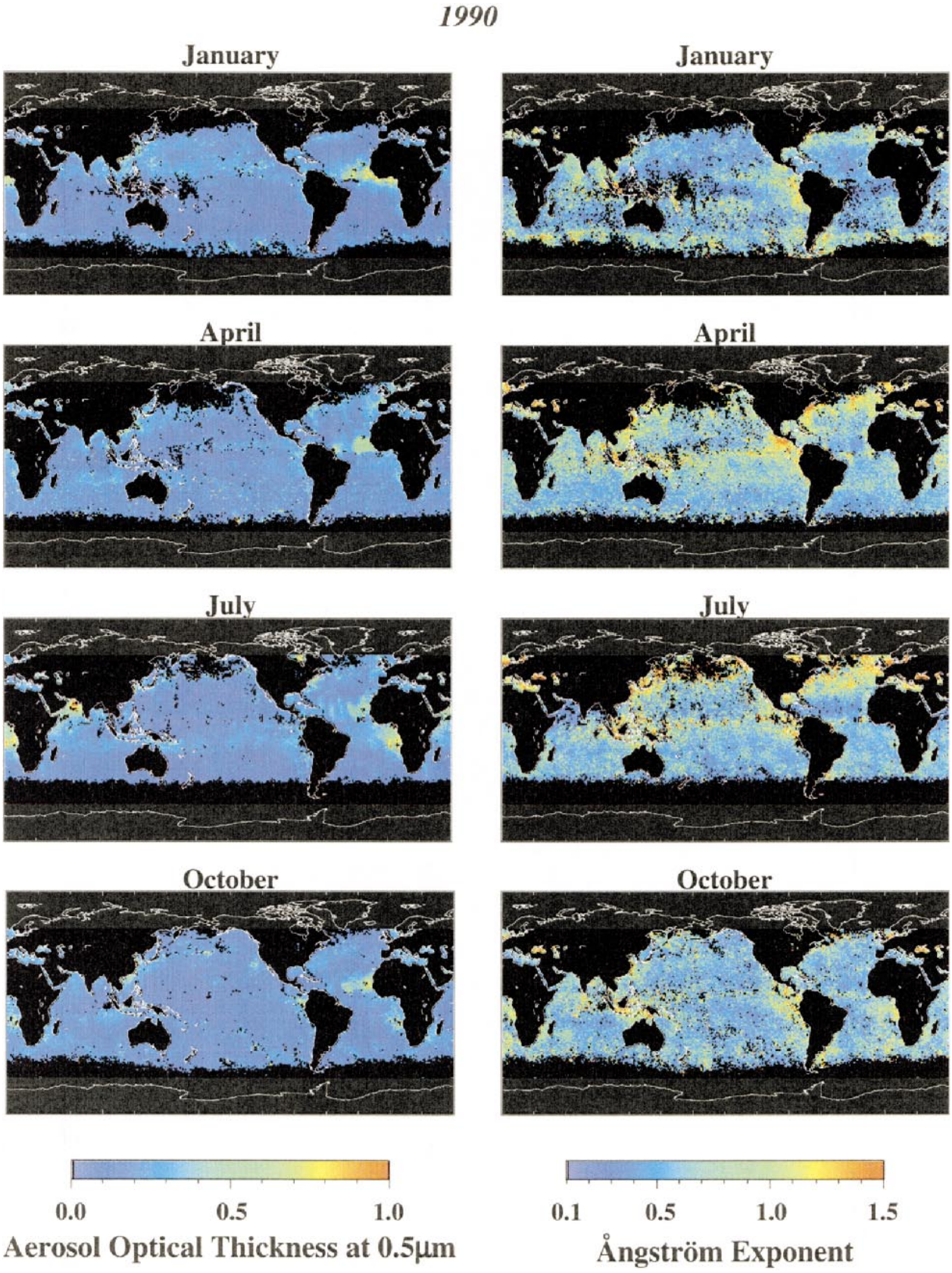

FIG. 10. Global distributions of $\tau_{a,\mathrm{sat}}$ and α_{sat} in Jan, Apr, Jul, and Oct 1990.

TABLE 3. Regional averages of satellite-retrieved aerosol optical thickness at 0.5 μm, $\tau_{a,\mathrm{sat}}$, and Ångström exponent, α_{sat}, in Jan, Apr, Jul, and Oct 1990.

	$\tau_{a,\mathrm{sat}}$					α_{sat}				
Region name	Jan	Apr	Jul	Oct	Ave	Jan	Apr	Jul	Oct	Ave
Open sea										
NE Pacific	0.18	0.19	0.13	0.19	0.17	0.41	0.71	0.80	0.57	0.62
NW Pacific	0.22	0.25	0.18	0.19	0.21	0.49	0.74	0.79	0.58	0.65
N Atlantic	0.19	0.23	0.20	0.19	0.20	0.68	0.94	1.00	0.60	0.81
EC Pacific	0.22	0.17	0.15	0.14	0.17	0.51	0.67	0.67	0.52	0.59
WC Pacific	0.22	0.14	0.12	0.10	0.15	0.35	0.63	0.73	0.56	0.57
SE Pacific	0.16	0.18	0.12	0.17	0.16	0.61	0.48	0.35	0.50	0.49
S Indian Sea	0.15	0.17	0.14	0.19	0.16	0.62	0.51	0.46	0.55	0.54
New Zealand	0.15	0.17	0.11	0.14	0.14	0.62	0.52	0.45	0.52	0.53
North America										
W US	0.16	0.16	0.15	0.20	0.17	0.49	0.90	0.73	0.52	0.66
E US	0.18	0.31	0.41	0.22	0.28	0.90	1.24	1.04	0.61	0.95
SE US	0.21	0.20	0.26	0.23	0.23	0.71	0.90	1.03	0.78	0.86
Central America										
C America	0.21	0.20	0.20	0.15	0.19	0.71	1.03	0.77	0.76	0.82
Caribbean	0.24	0.20	0.25	0.15	0.21	0.49	0.74	0.41	0.57	0.55
South America										
Peru	0.20	0.25	0.29	0.27	0.25	1.02	0.92	0.79	0.95	0.92
NE Brazil	0.34	0.29	0.21	0.20	0.26	0.46	0.62	0.63	0.57	0.57
E Brazil	0.11	0.18	0.15	0.17	0.15	0.43	0.60	0.70	0.54	0.57
Africa and the Middle East										
W Africa	0.30	0.25	0.32	0.33	0.30	0.43	0.62	0.43	0.46	0.49
Guinea	0.48	0.34	0.34	0.24	0.35	0.37	0.60	0.59	0.69	0.56
SW Africa	0.18	0.23	0.40	0.26	0.27	0.48	0.68	0.57	0.73	0.62
SE Africa	0.13	0.20	0.19	0.28	0.20	0.51	0.62	0.68	0.77	0.65
Arabia	0.23	0.19	0.61	0.23	0.32	0.78	0.68	0.31	0.63	0.60
Asia										
Bengal	0.28	0.26	0.31	0.17	0.26	0.78	0.82	0.46	0.70	0.69
Indonesia	0.14	0.17	0.20	0.23	0.19	0.75	0.83	0.81	0.72	0.78
New Guinea	0.13	0.17	0.24	0.16	0.18	0.60	0.86	0.81	0.80	0.77
S China Sea	0.35	0.28	0.20	0.28	0.28	0.65	1.01	0.82	0.72	0.80
China	0.36	0.36	0.25	0.36	0.33	0.76	1.02	1.09	0.86	0.93
Japan	0.24	0.27	0.23	0.21	0.24	0.51	0.92	1.12	0.55	0.78
Europe										
W Europe	0.16	0.30	0.21	0.17	0.21	0.78	0.86	0.82	0.54	0.75
NW Europe	0.14	0.34	0.29	0.19	0.24	0.90	1.04	1.26	0.67	0.97
Mediterranean	0.21	0.27	0.29	0.29	0.27	0.86	0.99	1.11	0.59	0.89
Black Sea	0.19	0.36	0.43	0.33	0.34	1.11	1.35	1.61	1.32	1.35
Caspian	0.21	0.30	0.40	0.21	0.28	1.03	1.38	1.18	1.02	1.15
N. Hemisphere	0.23	0.21	0.21	0.18	0.21	0.55	0.76	0.74	0.60	0.66
S. Hemisphere	0.14	0.18	0.18	0.17	0.17	0.57	0.61	0.56	0.57	0.58

as suggested by the fact that $\tau_{a,\mathrm{sat}}$ and α_{sat} in the Northern Hemisphere are larger than in the Southern Hemisphere. The seasonal variability of $\tau_{a,\mathrm{sat}}$ is different from that in the same regions obtained by Husar et al. (1997), which has a maximum in summer and a minimum in winter, as shown in Table 3. This difference may be caused by the difference in α in summer and winter from the fixed value of α used in the NOAA algorithm, that is, $\sim$1.0.

2) NORTH AMERICA, EUROPE, AND EASTERN ASIA

As shown in Fig. 12, both $\tau_{a,\mathrm{sat}}$ and α_{sat} remarkably increase in spring and/or summer on the east coast of North America, Europe, and eastern Asia, where strong sources of anthropogenic pollutant exist, corresponding to the regions labelled E US, SE US, W Europe, NW Europe, Mediterranean, Black Sea, Caspian, S China Sea, China, and Japan in the figure. In this case, α_{sat} reaches a value as large as 1.5. The summertime increase of the turbidity in these areas are caused by aerosol growth through the accumulation process, further growth of particles absorbing water vapor under high relative humidity condition, and stagnation due to weak horizontal wind velocity and weak vertical wind shear, as also suggested by numerical simulation of aerosol distribution we have performed, though not shown in this study. On the other hand, the correlation between

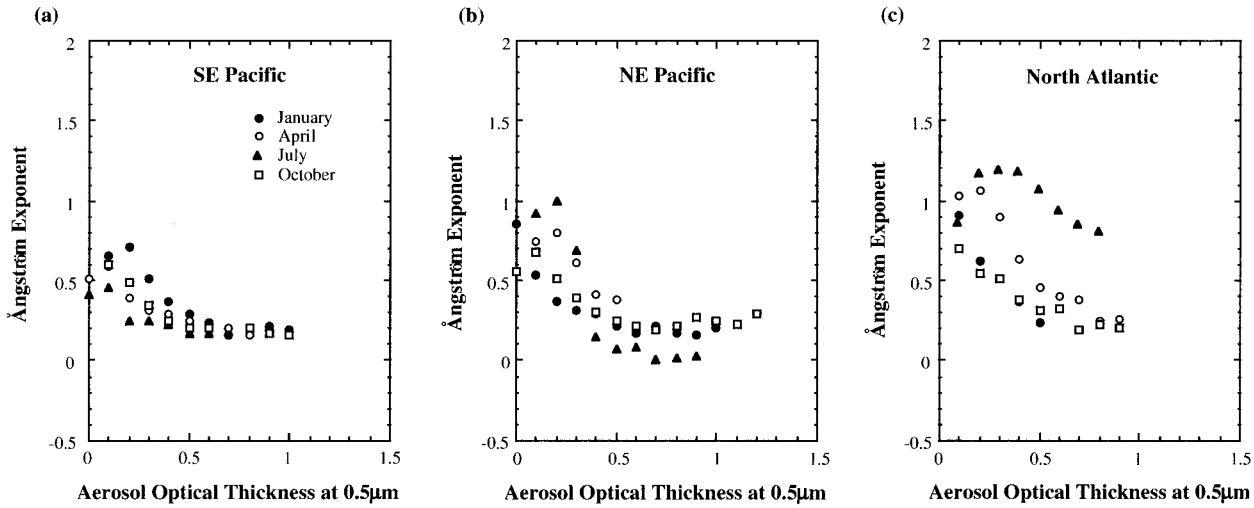

FIG. 11. Correlation patterns between $\tau_{a,\mathrm{sat}}$ and α_{sat} in (a) SE Pacific, (b) NE Pacific, and (c) N Atlantic as illustrated in Fig. 1.

$\tau_{a,\mathrm{sat}}$ and α_{sat} in areas such as E US, W Europe, and Japan in winter is similar to that of the open sea. The correlation in conspicuously polluted areas, such as China, Black Sea, and Caspian Sea, is similar in all seasons suggesting an accumulation process is dominant through the year.

3) AFRICA AND THE MIDDLE EAST

The impact of Saharan dust is significant over a large portion of the North Atlantic Ocean with long distance transportation by trade wind. Figure 13 shows that $\tau_{a,\mathrm{sat}}$ of W Africa is constantly large throughout the year, while α_{sat} takes almost a constant value about 0.5, which is characteristically small reflecting the large loading of desert dust. Such a characteristic relationship between τ_a and α has been observed by ground-based sunphotometry (Nakajima et al. 1989). The position of the Saharan dust plume shifts from south to north with the seasonal march of the ITCZ from winter to summer. This is one of the reasons why $\tau_{a,\mathrm{sat}}$ of Guinea increases in January as shown in Table 3. Another reason for the increase in $\tau_{a,\mathrm{sat}}$ will be an influence of biomass burning. It is reported that fires were observed by the Defense Meteorological Satellite Program (DMSP) imagery in the savannas south of the Sahara desert (Cahoon et al. 1992). Also, Cahoon et al. (1992) showed that from July to October the fire activity moves from western to eastern South Africa. This seasonal change in fire locations seems to be consistent with the characteristic increase of $\tau_{a,\mathrm{sat}}$ and α_{sat} in region SE Africa in October (Fig. 13b, Table 3), suggesting a generation of small accumulation mode particles. Relatively high values of the Ångström exponent may be partly caused by an effect of small biomass burning aerosols mixed with dust particles, which have almost zero exponent values.

Figure 13 clearly shows that the aerosol properties over the Arabian Sea in July is different from others,

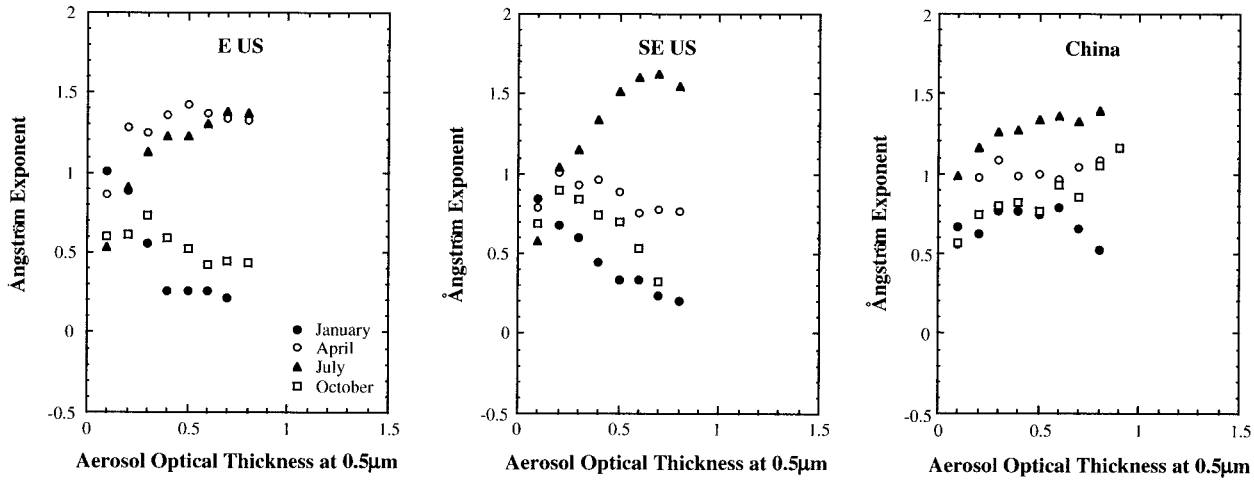

FIG. 12. Same as in Fig. 11 but for the regions (a) E US, (b) SE US, and (c) China.

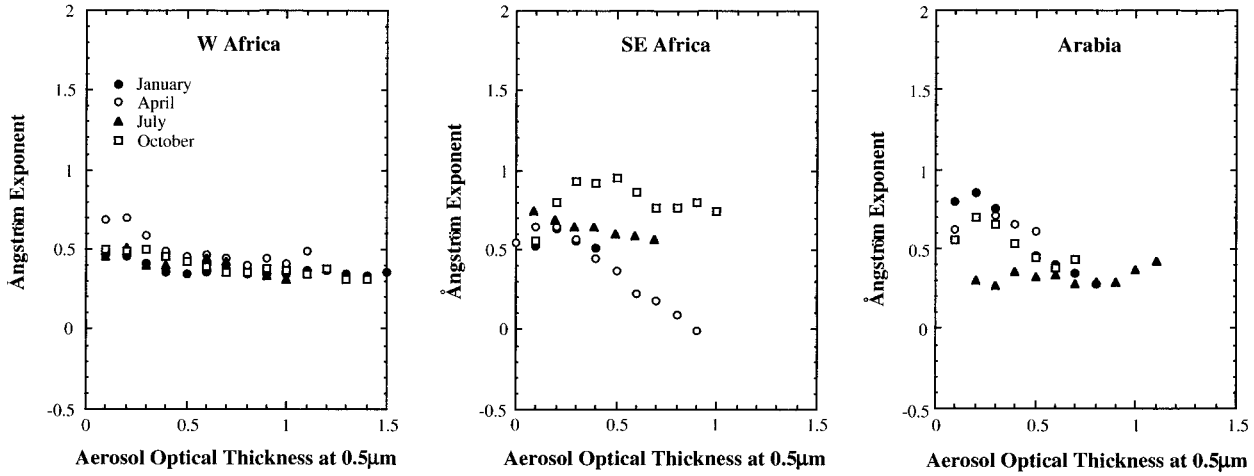

FIG. 13. Same as in Fig. 11 but for the regions (a) W Africa, (b) SE Africa, and (c) Arabia.

indicating mineral dust aerosols becomes dominant, taking the place of anthropogenic or oceanic aerosols, which are dominant in winter time.

4) CENTRAL AND SOUTH AMERICA

In April, we find conspicuously large α_{sat} in Central America that can be explained by an influence of biomass burning from the distribution of fires seen from space (Andreae 1992) and the analysis of UV absorbing aerosols using TOMS (Herman et al. 1997). It is difficult to attribute the large α to industrial aerosols since TOMS does not sense sulfate aerosols, which do not absorb UV radiation significantly. Such an agreement of aerosol classification by τ–α correlation pattern and TOMS UV absorbing aerosol distributions is also found in the Caribbean Sea shown in Fig. 14, where both methods suggest that this region is influenced by Saharan dust transported with the trade wind.

c. Zonal mean of $\tau_{a,\text{sat}}$ and α_{sat}

The zonal mean values of $\tau_{a,\text{sat}}$ and α_{sat} for each month are shown in Fig. 15. Some peak of $\tau_{a,\text{sat}}$ appears in the low-latitude zone between 20°S and 20°N, where there are large deserts and many biomass burning areas. Another peak occurs in the mid–high-latitude zone to the north of 40°N, where there are sources of anthropogenic aerosol emission from industrial areas. In the polluted zone $\tau_{a,\text{sat}}$ increases strongly, reaching a value as large as 0.25 in spring and summer. The average of $\tau_{a,\text{sat}}$ in the Northern Hemisphere is larger than that in the Southern Hemisphere by about 0.05. Compared to $\tau_{a,\text{sat}}$, α_{sat} stays in a relatively narrow range around 0.5 in most of latitudes other than northern high latitudes. The most interesting observation in the zonal mean profile of α_{sat} is its seasonal variations in the tropical zone between 20°S and 20°N and the high-latitude zone to the north of 40°N. The α_{sat} as well as $\tau_{a,\text{sat}}$ remarkably increases

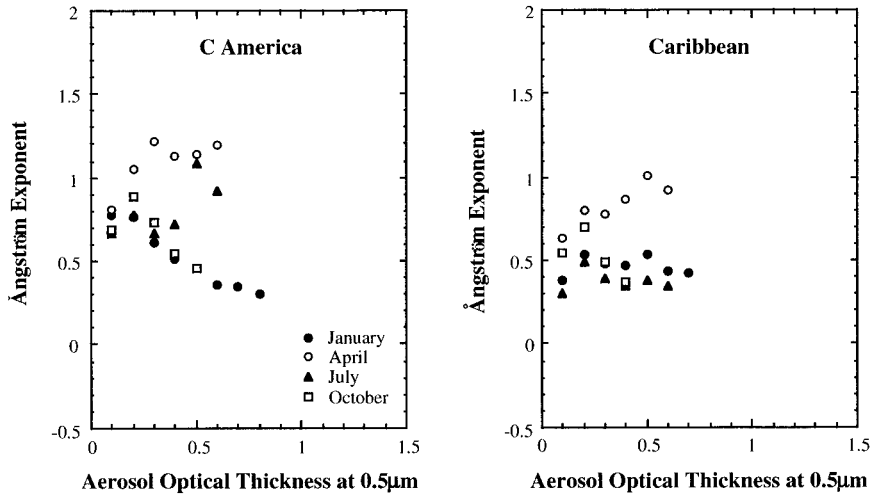

FIG. 14. Same as in Fig. 11 but for the regions (a) C America and (b) Caribbean.

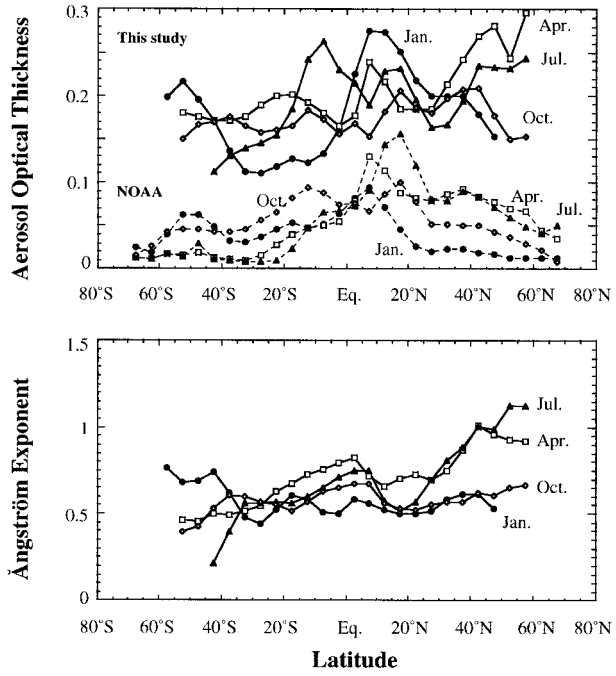

FIG. 15. Latitudal zonal mean profiles of Ångström parameters as a function of latitude from the present algorithm and the NOAA operational product.

in the high-latitude zone in spring and summer when a gas-to-particle conversion process is expected to be dominant. The zonal mean of α_{sat} in the tropical zone tends to have a peak around the equator and its pattern is different from that of $\tau_{a,\text{sat}}$. Both $\tau_{a,\text{sat}}$ and α_{sat} increase in July in the southern part of the zone, whereas $\tau_{a,\text{sat}}$ increases and α_{sat} decreases in January in the northern part of the zone. These characteristic seasonal changes indicate a difference in the dominant source for the peak in the tropical zone. The northern part of the peak of $\tau_{a,\text{sat}}$ may be caused by mineral dust aerosols, whereas the southern part caused by biomass burning aerosols. The increase of $\tau_{a,\text{sat}}$ and α_{sat} in January in the zone to the south of 30°S may be also caused by biological activities, as suggested by Chin et al. (1996) and Brechtel et al.(1998).

5. Discussion and conclusions

A validation study of our aerosol retrieval algorithm, which retrieves Ångström parameters ($\tau_{a,\text{sat}}$, α_{sat}) from NOAA AVHRR channel-1 and -2 radiance data, has been made by comparison with ground-based measurement data, which are selected from the AERONET sunphotometry dataset. We first observed that α_{sat} largely overestimate α_{gr} for $\alpha_{\text{gr}} < 0.45$ corresponding to mineral dust aerosols. We modified parameters not only for size distribution but also for sensor calibration to improve such overestimation. As a result, α_{sat} are decreased coming close to α_{gr} with a slight overestimation. It is also found a further improvement may be possible by assuming a wavelength-dependent imaginary index of refraction. Such an experience suggests that it is difficult to find a simple model to approximate various aerosol optical properties for global-scale remote sensing of aerosols only by changing the peak ratio of bimodal size distribution with fixed-mode radii and dispersions. We need further investigation to fully understand the problem. Such full validation is especially needed for AVHRR with the wide band width in channel 2, compared to recent radiometers, such as ADEOS OCTS and POLDER. In this regard, it is worth noting that Nakajima et al. (1999) and (Goloub et al. 1999) report a good correlation between OCTS and POLDER-derived values and ground-based measurement values of Ångström parameters if validation sites and timing are carefully selected.

We obtained global distributions of $\tau_{a,\text{sat}}$ and α_{sat} in January, April, July, and October 1990 with the modified aerosol model and sensor calibration constants. The most prominent aerosol layers detected from space are of mineral dust and biomass burning aerosols, consistent with previous studies (Husar et al. 1997; Herman et al. 1997). Analyses of distribution patterns of $\tau_{a,\text{sat}}$ and α_{sat} have shown that they spread over large areas with long-distance transportation of several thousand kilometers almost making a ''tropical belt of aerosols.'' Although not significant in the distribution of $\tau_{a,\text{sat}}$ the distribution of α_{sat} has clearly given us an evidence for aerosols originated from industrial activities in the northern mid–high latitudes and oceanic biological activities over the open sea areas. Aerosols from industrial sources certainly have an impact on the atmospheric condition in the Northern Hemisphere, especially in midlatitudes in spring and summer. The influence of biological activities on generating aerosols is evident by an increase of Ångström exponent in the high-latitudinal southern ocean in January. As mentioned above, seasonal variation of the Ångström parameters and correlation between them are thus useful for identifying aerosols from various sources. The differences in Ångström parameters, which are attributed to complicated distributions of land and human activities in the Northern Hemisphere, are estimated as $\Delta\tau = 0.05$ and $\Delta\alpha = 0.25$ in 1990. For comparison, we have plotted the zonal mean average of the optical thickness of the NOAA operational algorithm in Fig. 15. The profiles have shown that the effect of these two activities on the atmospheric turbidity is of similar order of magnitude making a characteristic distribution of the dominant particle size depending on latitude. It will be very important to validate this speculation about the competing effect of mineral dust and anthropogenic aerosols.

A long-term data analysis of NOAA AVHRR radiances with the present algorithm will make a large contribution to studies of the climate forcing of aerosols. Knowledge of the aerosol size distribution is important for calculating the number of aerosols, and hence, for

estimating the single scattering albedo and cloud–aerosol interaction. Extension of our method to multichannel radiances from current and future sensors, such as ADEOS OCTS, SeaWiFS, EOS MODIS, and *ADEOS-2* GLI, which have many channels in visible and/or infrared spectral regions, will be another challenge for us to make in near future to widen our knowledge on aerosol impacts to the earth's climate.

Acknowledgments. We are grateful to Dr. J. Tucker of NASA GSFC and Dr. R. Imasu of NIRE in ARGASS (AVHRR GAC dataset for Atmosphere and Surface Studies) project for providing us with AVHRR GAC data used in this study. We wish to extend our gratitude to Dr. L. L. Stowe of NOAA NESDIS for his valuable advice. The ancillary data used in this work for ozone amount are provided by TOMS Ozone processing Team of NASA and for surface wind velocity and water vapor amount by NCEP.

REFERENCES

Andreae, M. O., 1993: Global distribution of fires seen from space. *Eos, Trans. Amer. Geophys. Union,* **74,** 129–144.

Ångström, A., 1961: Techniques of determining the turbidity of the atmosphere. *Tellus,* **13,** 214–223.

Brechtel, R. J., S. M. Kreidenweis, and H. B. Swan, 1998: Air mass characteristics, aerosol particle number concentrations, and number size distributions at Macquarie Island during the First Aerosol Characterization Experiment (ACE 1). *J. Geophys. Res.,* **103,** 16 351–16 367.

Cahoon, D. R., Jr., B. J. Stocks, J. S. Levine, W. R. Cofer III, and K. P. O'Neill, 1992: Seasonal distribution of African savanna fires. *Nature,* **359,** 812–815.

Carlson, T. N., and R. S. Caverly, 1977: Radiative characteristics of Saharan dust at solar wavelengths. *J. Geophys. Res.,* **82,** 3141–3152.

Charlson, R. J., S. E. Schwartz, J. M. Hales, R. D. Cess, J. A. Coakley Jr., J. E. Hansen, and D. J. Hofmann, 1992: Climate forcing by anthropogenic aerosols. *Science,* **25,** 426–430.

Che, N., and J. C. Price, 1992: Survey of radiometric calibration results and methods for visible and near infrared channels of NOAA-7, -9, and -11 AVHRRs. *Remote Sens. Environ.,* **41,** 19–27.

Chin, M., D. J. Jacob, G. M. Gardner, M. S. Foreman-Fowler, P. A. Spiro, and D. L. Savoie, 1996: A global three-dimensional model of tropospheric sulfate. *J. Geophys, Res.,* **101,** 18 667–18 690.

Durkee, P. A., F. Pfeil, E. Frost, and R. Shema, 1991: Global analysis of aerosol particle characteristics. *Atmos. Environ,* **25A,** 2457–2471.

Goloub, P., D. Tanré, J. L. Deuzé, M. Herman, A. Marchand, and F. M. Bréon, 1999: Validation of the first algorithm applied for deriving the aerosol properties over the ocean using the POLDER/ADEOS measurements. *IEEE Trans. Geosci. Remote Sens.,* **37,** 1586–1596.

Gordon, H. R., and M. Wang, 1994: Retrieval of water-leaving radiance and aerosol optical thickness over the oceans with SeaWiFS: A preliminary algorithm. *Appl. Opt.,* **33,** 443–452.

Herman, J. R., P. K. Bhartia, O. Torres, C. Hsu, C. Seftor, and E. Celarier, 1997: Global distribution of UV-absorbing aerosols from Nimbus 7/TOMS data. *J. Geophys. Res.,* **102,** 16 911–16 922.

Higurashi, A., and T. Nakajima, 1999: Development of a two channel aerosol retrieval algorithm on global scale using NOAA AVHRR. *J. Atmos. Sci.,* **56,** 924–941.

Holben, B. N., and Coauthors, 1998: AERONET—A federated instrument network and data archive for aerosol characterization. *Remote Sens. Environ.,* **66,** 1–16.

Husar, R. B., J. M. Prospero, and L. L. Stowe, 1997: Characterization of tropospheric aerosols over the oceans with the NOAA advanced very high resolution radiometer optical thickness operational product. *J. Geophys. Res.,* **102,** 16 889–16 909.

Ignatov, A. M., L. L. Stowe, S. M. Sakerin, and G. K. Korotaev, 1995: Validation of the NOAA/NESDIS satellite aerosol product over the North Atlantic in 1989. *J. Geophys. Res.,* **100,** 5123–5132.

IPCC, 1996: *Climate Change 1995. The Science of Climate Change.* Cambridge University Press, 572 pp.

Kaufman, Y. J., and B. N. Holben, 1993: Calibration of the AVHRR visible and near-IR bands by atmospheric scattering, ocean glint and desert reflection. *Int. J. Remote Sens.,* **14,** 21–52.

——, and T. Nakajima, 1993: Effect of Amazon smoke on cloud microphysics and albedo-analysis from satellite imagery. *J. Appl. Meteor.,* **32,** 729–744.

——, and B. N. Holben, 1996: Hemispherical backscattering by biomass burning and sulfate particles derived from sky measurements. *J. Geophys. Res.,* **101,** 19 433–19 445.

Kiehl, J. T., and B. P. Briegleb, 1993: The relative role of sulfate aerosols and greenhouse gases in climate forcing. *Science,* **260,** 311–314.

Li, X., H. Maring, D. Savoie, K. Voss, and J. M. Prospero, 1996: Dominance of mineral dust in aerosol light-scattering in the North Atlantic trade winds. *Nature,* **380,** 416–419.

Mitchell, J. F. B., T. C. Johns, J. M. Gregory, and S. F. B. Tett, 1995: Climate response to increasing levels of greenhouse gases and sulphate aerosols. *Nature,* **376,** 501–504.

Moulin, C., F. Dulac, C. E. Lambert, P. Chazette, I. Jankowiak, B. Chatenet, and F. Lavenu, 1997a: Long-term daily monitoring of Saharan dust load over ocean using Meteosat ISCCP-B2 data 2. Accuracy of the method and validation using sun photometer measurements. *J. Geophys. Res.,* **102,** 16 959–16 969.

——, C. E. Lambert, F. Dulac, and U. Dayan, 1997b: Control of atmospheric export of dust from North Africa by the North Atlantic Oscillation. *Nature,* **387,** 691–694.

Nakajima, T., and M. D. King, 1990: Determination of the optical thickness and effective radius of clouds from reflected solar radiation measurements. Part I: Theory. *J. Atmos. Sci.,* **47,** 1878–1893.

——, and A. Higurashi, 1998: A use of two-channel radiances for an aerosol characterization from space. *Geophys. Res. Lett.,* **25,** 3815–3818.

——, M. Tanaka, M. Yamano, M. Shiobara, K. Arao, and Y. Nakanishi, 1989: Aerosol optical characteristics in the yellow sand events observed in May, 1982 in Nagasaki—Part II: Model. *J. Meteor. Soc. Japan,* **67,** 279–291.

——, G. Tonna, R. Rao, Y. Kaufman, and B. Holben, 1996: Use of sky brightness measurements from ground for remote sensing of particulate polydispersions. *Appl. Opt.,* **35,** 2672–2686.

——, A. Higurashi, K. Aoki, T. Endoh, H. Fukushima, M. Toratani, Y. Mitomi, B. G. Mitchell, and R. Furuin, 1999: Early phase analysis of OCTS radiance data for aerosol remote sensing, *IEEE Trans. Geosci. Remote Sens.,* **37,** 1575–1585.

Patterson, E. M., D. A. Gillette, and B. H. Stockton, 1977: Complex index of refraction between 300 and 700 nm for Saharan aerosols. *J. Geophys. Res.,* **82,** 3153–3160.

Rao, C. R. N., and J. Chen, 1995: Inter-satellite calibration linkages for the visible and near-infrared channels of the Advanced Very High Resolution Radiometer on the NOAA-7, -9, and -11 spacecraft. *Int. J. Remote Sens.,* **16,** 1931–1942.

Santer, B. D., and Coauthors, 1996: A search for human influences on the thermal structure of the atmosphere. *Nature,* **382,** 39–46.

Sokolik, I. N., and O. B. Toon, 1996: Direct radiative forcing by anthropogenic airborne mineral aerosol. *Nature,* **381,** 681–683.

——, A. Andronova, and T. C. Johnson, 1993: Complex refractive index of atmospheric dust aerosols. *Atmos. Environ.,* **16,** 2495–2502.

Stowe, L. L., R. M. Cavoy, and P. P. Pelliguino, 1992: Monitoring the Mt. Pinatubo aerosol layer with *NOAA-11*/AVHRR data. *Geophys. Res. Lett.,* **19,** 159–162.

Taylor, K. E., and J. E. Penner, 1994: Response of the climate system to atmospheric aerosols and greenhouse gases. *Nature,* **369,** 734–737.

Tegen, I., A. A. Lacis, and I. Fung, 1996: The influence on climate forcing of mineral aerosols from disturbed soils. *Nature,* **380,** 419–422.

Tomasi, C., V. Vitale, and E. Caroli, 1983: Sahara dust program—II. Determination of the vertical particulate mass loading by using extinction models based on Junge-type size distributions. *J. Aerosol Sci.,* **14,** 529–539.

Twomey, S. A., M. Piepgrass, and T. L. Wolfe, 1984: An assessment of the impact of pollution on global cloud albedo. *Tellus,* **36B,** 356–366.

van de Hulst, H. C., 1957: *Light Scattering by Small Particles.* Dover, 470 pp.

Yamauchi, T., 1995: Statistical analysis of atmospheric turbidity over Japan: The influence of three volcanic eruptions. *J. Meteor. Soc. Japan,* **73,** 91–103.